

## Hyperbolic lines and the stratospheric polar vortex

Tieh-Yong Koh<sup>a)</sup> and Bernard Legras<sup>b)</sup>

*Laboratoire de Météorologie Dynamique UMR8539, 24 Rue Lhomond, 75231 Paris Cedex 5, France*

(Received 8 January 2002; accepted 26 March 2002; published 20 May 2002)

The necessary and sufficient conditions for Lagrangian hyperbolicity recently derived in the literature are reviewed in the light of older concepts of effective local rotation in strain coordinates. In particular, we introduce the simple interpretation of the necessary condition as a constraint on the local angular displacement in strain coordinates. These mathematically rigorous conditions are applied to the winter stratospheric circulation of the southern hemisphere, using analyzed wind data from the European Center for Medium-Range Weather Forecasts. Our results demonstrate that the sufficient condition is too strong and the necessary condition is too weak, so that both conditions fail to identify hyperbolic lines in the stratosphere. However a phenomenological, nonrigorous, criterion based on the necessary condition reveals the hyperbolic structure of the flow. Another (still nonrigorous) alternative is the finite-size Lyapunov exponent (FSLE) which is shown to produce good candidates for hyperbolic lines. In addition, we also tested the sufficient condition for Lagrangian ellipticity and found that it is too weak to detect elliptic coherent structures (ECS) in the stratosphere, of which the polar vortex is an obvious candidate. Yet, the FSLE method reveals a clear ECS-like barrier to mixing along the polar vortex edge. Further theoretical advancement is needed to explain the apparent success of nonrigorous methods, such as the FSLE approach, so as to achieve a sound kinematic understanding of chaotic mixing in the winter stratosphere and other geophysical flows. © 2002 American Institute of Physics. [DOI: 10.1063/1.1480442]

**Transport plays an important role in the distribution of chemicals in the stratosphere (the layer of atmosphere between 12 and 55 km in altitude). This fact is clearly illustrated by, for instance, the formation of the Antarctic ozone hole every austral winter. In the extratropical stratosphere, chemical transport proceeds in quasihorizontal layers, where air parcels practically conserve entropy for up to about 3 weeks. Transport, stirring, and mixing in these isentropic layers is governed by the Lagrangian chaos generated by organized large-scale circulations (of several hundred kilometers and larger). The spatial organization of chaotic stirring is described by the main hyperbolic lines (i.e., the material lines that are locally the most attracting or repelling) forming at any time a skeleton of paths and lobes through the flow. Gradients of long-lived tracers tend to orient normal to and intensify along strongly attracting lines, thereby enhancing the mixing process by small-scale vertical circulations. At the same time, a strong vortical circulation exists in the winter polar region. The polar vortex exemplifies an elliptic coherent structure: its edge forms a partial barrier to mixing. Rigorous mathematical criteria were derived recently to characterize hyperbolic lines and elliptic coherent structures. In this paper, we review and test these criteria in a case study using stratospheric winds from the European Center for Medium-Range Weather Forecasts. Our work shows that these criteria**

**fail to pick out hyperbolic lines and elliptic coherent structures in the stratosphere, which are, however, readily identified with other less rigorous methods.**

### I. INTRODUCTION

A large number of chemical compounds in the atmosphere are long-lived species. As soon as the lifetime exceeds a few weeks, the large-scale distribution is to a large extent governed by transport from sources to sinks, and stirring and mixing. This observation is also valid for chemical and biological species in the ocean, and although the time scales are very different, for the chemical and mineralogical composition of the Earth's mantle. For a variety of reasons including the aspect ratio, stratification, and rotation, large-scale motion in the atmosphere and the ocean is mainly smooth and layerwise. This is particularly true in the stratosphere, the region of the atmosphere which extends from about 12 km in the midlatitudes and 18 km in the tropics up to 55 km. In this region, convective vertical motion is strongly inhibited by the stratification and radiatively induced vertical motion is typically of the order of 10 m per day under 30 km altitude. Smoothness is here associated with layerwise motion since it is well known that two-dimensional and quasigeostrophic flows are dominated by the large-scale structures. Consequently the stirring and mixing is more chaotic than turbulent in the sense that the time scales are not determined by the smallest spatial scales of motion, unlike the condition prevailing, say, in the combustion chamber of a rocket.

Two types of approaches have so far been developed to investigate the stirring properties of such flows. The statistical approach, rooted in the seminal work of Batchelor,<sup>1</sup> has

<sup>a)</sup>Present address: National University of Singapore, 10 Kent Ridge Crescent, Singapore 119 260, Republic of Singapore; electronic mail: tsikty@nus.edu.sg

<sup>b)</sup>Electronic mail: legras@lmd.ens.fr

recently shown considerable theoretical progress<sup>2,3</sup> leading to the prediction of the probability density functions of tracer gradients under a fairly wide range of physical hypothesis. This approach is relevant to the interpretation of the small-scale fluctuations that are observed from numerical simulations,<sup>4</sup> and from airborne measurements.<sup>5</sup>

Unlike eddies in a combustion chamber, atmospheric vortices are large, persistent, and cannot be considered only from a statistical standpoint. Hence the second approach that we will follow here addresses the deterministic and geometric properties of transport and stirring in the atmosphere.

A prominent example is that of the stratospheric polar vortex which is a strong cyclonic circulation in the polar region during winter in response to strong radiative cooling over the poles. This vortex is stronger and more stable in the Antarctic than in the Arctic. The Antarctic polar vortex has gained much recognition because it provides the conditions necessary for massive destruction of ozone, leading to the formation of the ozone hole. The polar vortex also serves as a paradigm for other similar issues, like the tropical barrier in the stratosphere and the subtropical jet in the troposphere.

An important property of the polar vortex that is instrumental to ozone destruction is its relative isolation from the midlatitudes: the polar air mass does not receive significant intrusions from midlatitude air masses.<sup>6–9</sup> Consequently, very different chemical conditions prevail inside and outside the vortex. The boundary between the vortex and its exterior is often seen as a very sharp transition in chemical mixing ratios measured by aircraft transects.<sup>10</sup> In this paper, we define the vortex edge to be at the location of the sharpest gradient in the mixing ratio of certain chemicals, e.g., nitrous oxide, surrounding the polar vortex. Another tracer, the potential vorticity (PV, see the definition in Sec. IV A), may be used in place of chemical mixing ratios to define the polar vortex edge. (The definition of the vortex edge based on tracer gradients usually requires further refinement to be fully operational but we do not need to enter into such complications here.) PV is not measured directly but is calculated from high-resolution simulations where an initial PV distribution is advected passively,<sup>11</sup> assuming that PV is materially conserved, an approximation that is generally valid over time scales of one to three weeks. These simulations all show that sharp PV gradients are often co-located with the sharp chemical tracer gradients observed from aircraft or balloon data. These findings have led to the idea that a dynamical barrier exists around the polar vortex which inhibits exchange with the midlatitudes.

In the standard context of dynamical systems, a barrier is an invariant torus on which trajectories do not disperse exponentially like in the surrounding chaotic regions.<sup>12</sup> In practice, studies have diagnosed the barrier effect of the polar vortex in terms of minimum Lyapunov exponent,<sup>13</sup> minimum stretching of material lines,<sup>14</sup> and minimum effective diffusivity.<sup>15</sup> These minima are, however, much broader than the actual width of the high-gradient region between the vortex and the exterior, which can be as small as 3 km according to aircraft data.<sup>10</sup>

The dynamical barrier around the polar vortex is not perfect, as it is constantly disturbed by planetary waves

(which are weaker in the southern hemisphere than in the northern hemisphere, and hence the higher stability of the vortex). As a result, the vortex is continuously eroded into filaments which are expelled into the surf zone<sup>16</sup> (so called because it is the midlatitude region stirred by breaking Rossby waves). It is generally considered, based on observations and trajectory calculations, that filament-shedding in the stratosphere is essentially a one-way process: filaments of polar air are shed from the vortex but air parcels from the surf zone hardly penetrate into the vortex through layerwise isentropic motion. The vortex interior is mainly fed through slow diabatic descent. Vortex erosion is a very efficient mechanism to generate and maintain high tracer gradients, as shown by numerical experiments and theory in two-dimensional turbulence.<sup>17,18</sup> Therefore, vortex coherence and erosion, and relatedly the distribution of tracers, should be better understood from the stirring properties of the stratospheric flow.

Early attempts to characterize the stirring properties of a two-dimensional flow<sup>19,20</sup> were based on the eigenvalues of the velocity gradient tensor, distinguishing areas where particle separation grows exponentially from other areas where the separation oscillates. This is the so-called Okubo–Weiss criterion. When applied to describe a particle trajectory, this criterion relies on the assumption that the velocity gradient tensor is frozen during the motion of a fluid parcel, a condition which is hardly met, even by the simplest flows.<sup>21</sup> Considerable improvements have been achieved recently by considering the separation of particles in a reference frame rotating with the strain axes.<sup>22–24</sup> This is a significant step toward a Lagrangian description which is needed since stretching of a fluid parcel results from the history of strain along its trajectory.<sup>25</sup> Other techniques are based on the elongation of a contour line, usually chosen as a contour of potential vorticity.<sup>14</sup>

The theory of Hamiltonian dynamical systems indicates that stirring in a smooth incompressible flow is best described by the knowledge of hyperbolic points and the intricate tangle of the associated stable and unstable manifolds. Most of the applications have been devoted to the study of periodic flows where powerful methods like the Poincaré map can be used.<sup>12,26,27</sup> It is only recently that the quasiperiodic and the aperiodic situations have been considered.<sup>28–34</sup> In the aperiodic case, which is obviously more relevant from the perspective of transport and stirring in geophysical flows, the hyperbolic invariant manifolds may or may not cross; if they cross, they may only have a finite number of crossings; and the hyperbolic trajectories may be of finite duration. Several techniques that have been used in the aperiodic case try to map the hyperbolic structures from various estimators of stretching like the finite-time Lyapunov exponents<sup>35</sup> or patchiness.<sup>36</sup> In the following we will use a method called the finite-size Lyapunov exponent which shows some high skill at detecting the hyperbolic structure.<sup>37</sup>

A particularly interesting approach is a series of recent works by Haller,<sup>32,33,38,39</sup> who has obtained rigorous results on the characterization of attracting and repelling hyperbolic material lines over finite-time intervals. Such lines are the finite-time generalizations of unstable and stable hyperbolic

manifolds which they approach as time goes to infinity. The mathematical results of Haller, which are described in more detail in Sec. III, provide necessary and sufficient criteria for a material trajectory to belong to a hyperbolic line. Unfortunately, the necessary and the sufficient criteria are still different and do not provide a narrow bracketing of the hyperbolic lines in all cases, although they perform very well in some idealized problems.

The goal of this paper is to present the application of the most recent version of Haller’s results<sup>39</sup> within the context of the polar vortex flow.

In Sec. II, we review the existing criteria for local hyperbolic and elliptic properties. In Sec. III, we summarize and interpret Haller’s results for Lagrangian hyperbolic and elliptic structures. Section IV presents our computational methods and data. Section V presents and discusses the results of applying Haller’s conditions to the polar vortex. Section VI compares those results with results from the finite-size Lyapunov exponent (FSLE) calculations. Section VII states our conclusions and offers further discussions.

## II. LOCALLY HYPERBOLIC AND ELLIPTIC REGIONS

### A. Okubo–Weiss criterion

In a two-dimensional velocity field  $\mathbf{v}$ , the time evolution of the displacement element  $\delta\mathbf{s}$  from particle A to a close neighboring particle B is given by

$$\frac{D}{Dt} \delta\mathbf{s} = \delta\mathbf{s} \cdot \nabla\mathbf{v},$$

where  $\nabla\mathbf{v}$  is the velocity differential matrix of the vector  $\mathbf{v}$ . In stratified geophysical flows, the two-dimensional spatial domain is a spherical surface labeled by longitude–latitude coordinates  $(\lambda, \varphi)$ . We may consider  $\delta\mathbf{s}$  and  $\mathbf{v}$  to exist in the tangential plane spanned by the unit vectors  $(\hat{\lambda}, \hat{\varphi})$  at the location of particle A. Thus (cf. Appendix 2 of Ref. 40)

$$\delta\mathbf{s} \equiv \begin{pmatrix} R \cos \varphi & \delta\lambda \\ R & \delta\varphi \end{pmatrix}, \quad \mathbf{v} \equiv \begin{pmatrix} R \cos \varphi & \dot{\lambda} \\ R & \dot{\varphi} \end{pmatrix},$$

$$\nabla\mathbf{v} \equiv \begin{pmatrix} -\dot{\varphi} \tan \varphi + \frac{\partial \dot{\lambda}}{\partial \lambda} & -\dot{\lambda} \sin \varphi + \cos \varphi \frac{\partial \dot{\lambda}}{\partial \varphi} \\ \dot{\lambda} \sin \varphi + (\cos \varphi)^{-1} \frac{\partial \dot{\varphi}}{\partial \lambda} & \frac{\partial \dot{\varphi}}{\partial \varphi} \end{pmatrix},$$

where  $R$  is the Earth’s radius.  $\nabla\mathbf{v}$  may be split as  $\nabla\mathbf{v} \equiv \mathbf{S} + \mathbf{O}$  where the strain matrix  $\mathbf{S}$  is the symmetric component, and the rotation matrix  $\mathbf{O}$  is the antisymmetric component:

$$\mathbf{S} \equiv \begin{pmatrix} a & b \\ b & c \end{pmatrix}, \quad \mathbf{O} \equiv \begin{pmatrix} 0 & -\dot{\lambda} \sin \varphi - \Omega \\ \dot{\lambda} \sin \varphi + \Omega & 0 \end{pmatrix},$$

where

$$a \equiv \partial \dot{\lambda} / \partial \lambda - \dot{\varphi} \tan \varphi, \tag{1}$$

$$b \equiv \frac{1}{2} \left[ (\cos \varphi)^{-1} \frac{\partial \dot{\varphi}}{\partial \lambda} + \cos \varphi \frac{\partial \dot{\lambda}}{\partial \varphi} \right], \tag{2}$$

$$c \equiv \frac{\partial \dot{\varphi}}{\partial \varphi}, \tag{3}$$

$$\Omega \equiv \frac{1}{2} \left[ (\cos \varphi)^{-1} \frac{\partial \dot{\varphi}}{\partial \lambda} - \cos \varphi \frac{\partial \dot{\lambda}}{\partial \varphi} \right]. \tag{4}$$

$\Omega$  is the rotation rate relative to the basis set  $(\hat{\lambda}, \hat{\varphi})$ , which itself is rotating at a rate of  $\dot{\lambda} \sin \varphi$  in the tangential plane. For the rest of this paper, we shall assume that the flow is nondivergent so that  $a = -c$ .

The sign of  $\det \nabla\mathbf{v}$  characterizes the flow in the neighborhood of particle A, assuming that  $\nabla\mathbf{v}$  is quasiconstant with time.<sup>19,20</sup> Thus, the flow is separated into elliptic, parabolic and hyperbolic regions:

$$\det \nabla\mathbf{v} = (\dot{\lambda} \sin \varphi + \Omega)^2 - a^2 - b^2 \begin{cases} > 0 & \text{elliptic} \\ = 0 & \text{parabolic} \\ < 0 & \text{hyperbolic} \end{cases}. \tag{5}$$

Equation (5) is sometimes called the Okubo–Weiss criterion.

Note that  $\det \nabla\mathbf{v}$  is not invariant under rotation of the frame of reference:  $\dot{\lambda} \rightarrow \dot{\lambda} + \text{constant}$ , due to the presence of the  $\dot{\lambda} \sin \varphi$  term in Eq. (5). Hence, the results obtained from applying the Okubo–Weiss criterion in two differently rotating frames will not agree. Thus, one has to decide in which frame the Okubo–Weiss criterion is to be applied. For example, should the Earth’s frame be used? Or perhaps a frame moving with some average flow velocity is more suitable? In general, it is difficult to choose any one reference frame over another based on the flow kinematics alone.

### B. Using strain coordinates

Dresselhaus and Tabor<sup>41</sup> suggested the use of *strain coordinates*—i.e., a local frame moving with the eigenvectors of the strain matrix  $\mathbf{S}$ —in analyzing the kinematics of material elements in a flow field. As the set of eigenvectors of  $\mathbf{S}$  along every trajectory in the flow rotates at its own rate, each particle in the flow is really analyzed in its own frame of reference. Thus, the question of an overall frame of reference for the flow is circumvented.

The strain matrix  $\mathbf{S}$  has orthonormal eigenvectors  $E_+$  and  $E_-$  belonging to eigenvalues  $\sigma$  and  $-\sigma$ , where  $\sigma$  is the rate of strain:

$$\sigma = \sqrt{a^2 + b^2}. \tag{6}$$

$E_+$  makes an angle  $\vartheta(t) \in [-\pi/2, \pi/2]$  with the unit vector  $\hat{\lambda}$ , where  $\vartheta$  is given implicitly by  $a = \sigma \cos 2\vartheta$  and  $b = \sigma \sin 2\vartheta$ . In strain coordinates, the rotation rate  $\Omega_{\text{eff}}$  of the local flow—coined the *effective rotation rate* in Ref. 41—appears as

$$\Omega_{\text{eff}} = \Omega - \dot{\vartheta}, \tag{7}$$

where  $\dot{\vartheta}$  is the rotation rate of the strain axes relative to  $\hat{\lambda}$  along a particle trajectory:

$$\dot{\vartheta} = \frac{1}{2\sigma^2} (ab - \dot{a}b). \tag{8}$$

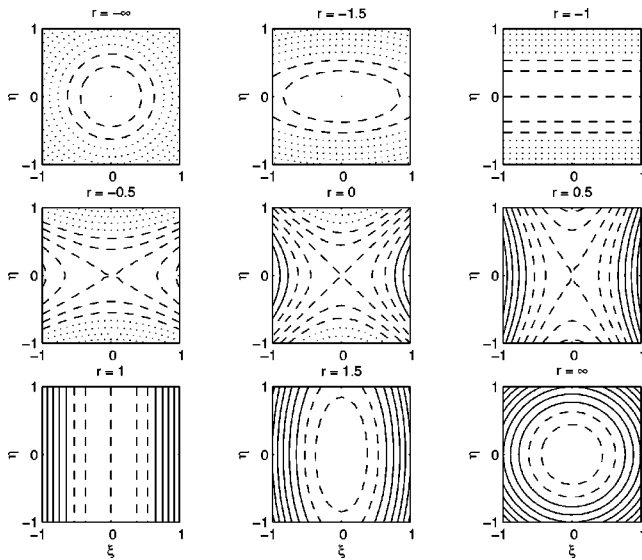


FIG. 1. The streamfunction  $\psi$  as  $r \equiv \Omega_{\text{eff}}/\sigma$  varies. [Let  $\xi$  and  $\eta$  be nondimensionalized infinitesimal displacements from a particle A in the zonal and meridional directions, respectively. Then,  $\psi \equiv (1+r^2)^{-1/2}(\psi_S+r\psi_R)$ , where  $\psi_S \equiv (\xi^2-\eta^2)/2$  and  $\psi_R \equiv (\xi^2+\eta^2)/2$ , where  $r$  is parameter in the HKOW criterion. Note that  $\psi$  is contoured at intervals of 0.1. Key: dotted line  $\leq -0.3$ ,  $-0.2 \leq$  dashed line  $\leq 0.2$ , and solid line  $\geq 0.3$ .]

More recently, Hua and Klein<sup>22</sup> and Lapeyre *et al.*<sup>23,24</sup> applied the Okubo–Weiss criterion in strain coordinates, and distinguished three regions of flow according to the parameter  $r$ :

$$r \equiv \Omega_{\text{eff}}/\sigma, \tag{9}$$

$$|r| \begin{cases} > 1 & \text{elliptic} \\ = 1 & \text{parabolic} \\ < 1 & \text{hyperbolic} \end{cases} \tag{10}$$

The above is sometimes called the Hua–Klein–Okubo–Weiss criterion, which we abbreviate as the *HKOW criterion*. As  $\sigma$  and  $\Omega_{\text{eff}}$  are invariant to the transformation  $\lambda \rightarrow \lambda + \text{constant}$ , the HKOW criterion is independent of the rotation of the reference frame.

Figure 1 depicts the morphology of the local flow field in strain coordinates as a function of  $r$ . The strain eigenvectors  $E_{\pm}$  are  $\pm 45^\circ$  lines in Fig. 1. Two significant features about the local flow in strain coordinates must be highlighted for the arguments in Sec. III.

- (1) For  $|r| > 1$ , the minimum angular speed around a trajectory occurs along the major axis of the elliptical flow pattern. It is readily shown to have a value of  $|\Omega_{\text{eff}}| - \sigma$ .
- (2) Even as  $r$  changes with time, the horizontal and vertical axes in Fig. 1 always experience no extension or compression. They constitute the *zero-strain set*.<sup>39</sup> The zero strain set divides the local flow field into four quadrants. In two quadrants, particles always recede from the origin, while in the other two quadrants, particles always approach the origin.

Note that the “EPH” partition of Haller<sup>39</sup> is actually equivalent to the HKOW criterion, but instead of using the parameter  $r$ , the EPH partition is defined in terms of fluid fluxes across the zero-strain set.

### III. LAGRANGIAN HYPERBOLICITY AND ELLIPTICITY

As  $r$  changes nontrivially along a particle trajectory owing to variations of  $\sigma$ ,  $\dot{\lambda}$  and/or  $\Omega$ , a particle may experience different local flow at different times: sometimes hyperbolic, sometimes parabolic, and sometimes elliptic. So how does one ascribe the notions of Lagrangian hyperbolicity and ellipticity to a particle trajectory? The approach adopted in this paper to answer this question is reviewed in the following. A different approach, which yields results that are not invariant to the transformation  $\lambda \rightarrow \lambda + \text{constant}$ , can be found in Ref. 42.

We quote from Haller<sup>39</sup> the following definitions: over a finite time interval  $I$ ,

- (1) A material line is *repelling* if all infinitesimal perturbations transverse to it strictly increase throughout  $I$  as time flows forward.
- (2) A material line is *attracting* if all infinitesimal perturbations transverse to it strictly increase throughout  $I$  as time flows backward.
- (3) A hyperbolic material line is either an attracting or a repelling material line.
- (4) An elliptic material line is not hyperbolic, and stays in an elliptic region throughout  $I$ .

In this paper, we shall say that a trajectory is hyperbolic over  $I$  if it is contained in a hyperbolic line throughout  $I$ , and that it is elliptic over  $I$  if it is contained in an elliptic line throughout  $I$ .

A notable contribution in Haller<sup>39</sup> is that separate necessary and sufficient conditions for hyperbolic and elliptic trajectories were derived. We paraphrase these conditions below for a finite time interval  $I$ .

*Sufficient condition for Lagrangian hyperbolicity.* Suppose a trajectory  $s(t)$  does not leave a hyperbolic region (where  $|r| < 1$ ) for  $t \in I$ . Then the trajectory is hyperbolic over  $I$ .

*Necessary condition for Lagrangian hyperbolicity.* Suppose a trajectory  $s(t)$  is hyperbolic over  $I$ . Then, the following are true.

- (1) The trajectory can only be in parabolic regions (where  $|r| = 1$ ) at isolated time instances.
- (2) If  $I_E \subset I$  denotes any time interval over which the trajectory stays in an elliptic region (where  $|r| > 1$ )—there can be more than one such time interval  $I_E$ —then

$$\int_{I_E} |\phi_0(s(t), t)| dt < \frac{\pi}{2}, \tag{11}$$

where

$$|\phi_0| = |\Omega_{\text{eff}}| - \sigma. \tag{12}$$

(The expression for  $\phi_0$  in Ref. 39 is actually more complicated, and is based on a different physical notion than the

one described in the following. Nevertheless, Haller’s  $|\phi_0|$  is equivalent to the above-given expression, as demonstrated in the Appendix.)

*Sufficient condition for Lagrangian ellipticity.* Suppose a trajectory  $\mathbf{s}(t)$  stays in an elliptic region (where  $|r| > 1$ ) throughout  $I$  and

$$\int_I |\phi_0(\mathbf{s}(t), t)| dt \geq \frac{\pi}{2}. \tag{13}$$

Then the trajectory is elliptic over  $I$ .

The reader is referred to Ref. 39 for the mathematical proofs of the above-given conditions. In the present paper, we provide a simple geometric understanding of  $|\phi_0|$  and the integral constraints in inequalities (11) and (13).

From the end of Sec. II B,  $|\phi_0|$  in Eq. (12) is evidently the minimum angular speed of neighboring particles about the trajectory  $\mathbf{s}(t)$  at time  $t$ . Hence, the integral  $\int_J |\phi_0(\mathbf{s}(t), t)| dt$  is the minimum angular distance that any neighboring particle travels around the trajectory  $\mathbf{s}(t)$  over the time interval  $J$ .

Therefore,  $\int_J |\phi_0(\mathbf{s}(t), t)| dt \geq \pi/2$  means that, during the interval  $J$ , all neighboring particles around  $\mathbf{s}$  would at some point leave their original quadrant that is demarcated by the zero strain set. So no neighboring particle approaches or recedes from the trajectory  $\mathbf{s}$  monotonically over  $J$ . Hence, by definition, the trajectory  $\mathbf{s}$  cannot be hyperbolic over  $J$ . Thus,

- (1) for the trajectory  $\mathbf{s}$  staying in an elliptic region over time interval  $I$ , the inequality (13) implies that the trajectory  $\mathbf{s}$  is not hyperbolic and hence elliptic over  $I$ ;
- (2) violation of inequality (11) for any  $I_E \subset I$  implies that the trajectory  $\mathbf{s}$  is not hyperbolic over  $I$ . By contraposition,  $\mathbf{s}$  being hyperbolic over  $I$  implies inequality (11) for all  $I_E \subset I$ .

#### IV. COMPUTATIONAL METHODS

##### A. Treatment of the stratospheric flow

Analyzed winds in the lower stratosphere from the European Center for Medium-range Weather Forecasts (ECMWF) were interpolated onto isentropic levels using a smooth interpolation scheme, the Akima scheme,<sup>43</sup> which minimizes spurious over- and under-shoots, unlike the cubic spline. Subsequent work was focused on the 500 K isentropic surface, which lies in the lower stratosphere.

Next, the irrotational wind component was put to zero to yield the nondivergent wind field  $(u, v)$ . This procedure is necessary because the above-mentioned theoretical analyses assume two-dimensional nondivergent flow. We are assuming that the irrotational wind (on isentropic surfaces) plays a minor role in the chaotic dynamics of tracer filaments in the stratosphere over a period of 2–3 weeks.

The absolute vorticity  $\zeta_\theta$  normal to isentropic surfaces was also computed from the ECMWF analyzed wind data. The distribution of  $\zeta_\theta$  was used to elucidate the position and internal structure of the polar vortex, because it is directly related to the isentropic nondivergent wind used in our diag-

noses of hyperbolic and elliptic trajectories.  $\zeta_\theta$  is the curl of the nondivergent wind along isentropic surfaces, written formally as

$$\zeta_\theta = [R(1 - \mu^2)]^{-1} \left[ \left( \frac{\partial V}{\partial \lambda} \right)_\theta - (1 - \mu^2) \left( \frac{\partial U}{\partial \mu} \right)_\theta \right], \tag{14}$$

where  $\mu \equiv \sin \varphi$ ,  $U \equiv u \cos \varphi$  and  $V \equiv v \cos \varphi$ . In contrast, Ertel potential vorticity  $\mathcal{P}$  is given by

$$\mathcal{P} = -g \zeta_\theta \frac{\partial \theta}{\partial p}.$$

$\mathcal{P}$  contains additional information on the vertical potential temperature profile, which is not considered in our work with the two-dimensional nondivergent wind field. Hence,  $\zeta_\theta$  is more useful for understanding the relation between vortex structure and the wind field, while  $\mathcal{P}$  is the actual dynamical tracer that is conserved on a time scale of a few weeks in the lower stratosphere.

##### B. Calculation of $r$

The isentropic nondivergent winds  $(u, v)$  were used to advect a grid of particles initially placed one degree apart (in both north–south and east–west directions) and spanning the region south of 25°S. This was done by solving advection equations, written formally as

$$\dot{\lambda} = \frac{U(\lambda(t), \varphi(t), t)}{R(1 - \mu^2)}, \quad \dot{\varphi} = \frac{V(\lambda(t), \varphi(t), t)}{R(1 - \mu^2)^{1/2}},$$

using the fourth-order Runge–Kutta method with a time step of 30 min. The  $(U, V)$  at each particle’s position  $(\lambda(t), \varphi(t))$  at time  $t$  were obtained using bilinear interpolation from the values of  $(U, V)$  on the ECMWF Gaussian grid.

To compute the rotation  $\Omega$  relative to the  $\hat{\lambda}$  axis, we rewrite Eq. (4) as

$$\Omega = \frac{1}{2R(1 - \mu^2)} \left[ \frac{\partial V}{\partial \lambda} - (1 - \mu^2) \frac{\partial U}{\partial \mu} - 2\mu U \right]. \tag{15}$$

To compute the strain rate  $\sigma$  from Eq. (6), we need to rewrite Eqs. (1)–(3) for nondivergent flows as

$$a = \frac{1}{2}(a - c) = \frac{1}{2R(1 - \mu^2)} \left[ \frac{\partial U}{\partial \lambda} - (1 - \mu^2) \frac{\partial V}{\partial \mu} - 2\mu V \right], \tag{16}$$

$$b = \frac{1}{2R(1 - \mu^2)} \left[ \frac{\partial V}{\partial \lambda} + (1 - \mu^2) \frac{\partial U}{\partial \mu} + 2\mu U \right]. \tag{17}$$

Both  $\Omega$  and  $\sigma$  were calculated on the same Gaussian grid as  $(U, V)$ , with the gradients of  $(U, V)$  evaluated spectrally first. Bilinear interpolation was used to obtain values  $\Omega$  and  $\sigma$  at each particle’s position.  $\dot{a}$  and  $\dot{b}$  were calculated by a backward-difference scheme using values of  $a$  and  $b$  along a particle trajectory over consecutive time steps. The rotation rate  $\dot{\theta}$  of the strain axes relative to the  $\hat{\lambda}$  axis was then computed using Eq. (8). Finally  $\Omega_{\text{eff}}$  and  $r$  were computed for each particle at every time step using Eqs. (7) and (9),

respectively. The HKOW criterion in Eq. (10) was used to determine if each particle was in an elliptic, parabolic, or hyperbolic region.

**C. Evaluation of Haller’s conditions**

From the sufficient condition for hyperbolic trajectories, we see that any particle that is in a hyperbolic region at time  $T$  must be hyperbolic over the time interval  $[T - \tau_b, T + \tau_f]$ , where  $T - \tau_b$  is the time it enters the hyperbolic region (i.e.,  $|r|$  changes from  $\geq 1$  to  $< 1$ ), and  $T + \tau_f$  is the time it leaves the hyperbolic region (i.e.,  $|r|$  changes from  $< 1$  to  $\geq 1$ ).  $\tau_f$  and  $\tau_b$  are computed via forward- and backward-time advection of the particles, respectively, from time  $T$ . Therefore, for each particle in a hyperbolic region at time  $T$ , we obtain

- (1) the length of time  $(\tau_b + \tau_f)$  for which the particle satisfies the sufficient condition, i.e., for which it is known to be hyperbolic;
- (2) the “strength” of the hyperbolicity, as measured by the integral  $\int_{T-\tau_b}^{T+\tau_f} \Lambda dt$  where  $\Lambda \equiv \sqrt{\sigma^2 - \Omega_{\text{eff}}^2}$  is the positive eigenvalue of the velocity differential matrix  $\nabla \mathbf{v}_{\text{eff}}$  in strain coordinates.

As regards the necessary condition for hyperbolic trajectories, the integral on the left-hand side of inequality (11) clearly increases monotonically with  $t_n$ , for  $I_E = [T, T + t_n]$  or  $[T - t_n, T]$ . Thus, a particle that is in an elliptic region at the initial time  $T$  will satisfy the necessary condition until the time  $T + \tau_n$  in forward-time advection, or the time  $T - \tau_n$  in backward-time advection, when the integral reaches the value of  $\pi/2$ . If the integral does not reach  $\pi/2$  before the particle leaves the elliptic region (i.e.,  $|r|$  changes from  $> 1$  to  $\leq 1$ ), or if the particle is not in an elliptic region at the initial time  $T$ , then the necessary condition is satisfied until the integral eventually does reach  $\pi/2$  at a later or earlier time (for forward- and backward-time advection, respectively) when the particle is in an elliptic region again. (Note: The value of the integral is reset to zero every time the particle leaves an elliptic region.) Hence, for *all* particles at time  $T$ , we separately obtain the following for forward- and backward-time advection.

- (1) The length of time  $\tau_n$  for which the necessary condition is satisfied, i.e., for which the particle may possibly be hyperbolic.
- (2) The “strength” of the hyperbolicity, as indicated roughly by the integral  $\int_I \Lambda dt$ , where  $I = [T, T + \tau_n]$  (for forward-time advection) or  $I = [T - \tau_n, T]$  (for backward-time advection), and

$$\Lambda \equiv \begin{cases} \sqrt{\sigma^2 - \Omega_{\text{eff}}^2} & \text{if } |r| < 1 \\ 0 & \text{otherwise} \end{cases} \quad (18)$$

From the sufficient condition for elliptic trajectories, we see that any particle that is in an elliptic region at time  $T$  must be elliptic over the time interval  $I = [T - \tau_b, T + \tau_f]$ , where  $T - \tau_b$  is the time it enters the elliptic region (i.e.,  $|r|$  changes from  $\leq 1$  to  $> 1$ ), and  $T + \tau_f$  is the time it leaves the elliptic region (i.e.,  $|r|$  changes from  $> 1$  to  $\leq 1$ ), provided

that inequality (13) is satisfied.  $\tau_f$  and  $\tau_b$  are computed, respectively, via forward- and backward-time advection of the particles. Therefore, for each particle in an elliptic region at time  $T$ , we compute

- (1) the length of time  $(\tau_b + \tau_f)$  for which the particle stays in an elliptic region;
- (2) the “strength” of the ellipticity, as measured by the integral  $\int_I |\phi_0| dt$  where  $I = [T - \tau_b, T + \tau_f]$ . Then, we pick out those particles for which  $\int_I |\phi_0| dt \geq \pi/2$ , i.e., which satisfies the sufficient condition for elliptic trajectories. These are the known elliptic trajectories.

**V. RESULTS**

Figure 2 shows the distribution of potential vorticity  $\mathcal{P}$  and absolute vorticity  $\zeta_\theta$  on the 500 K isentropic surface in the southern extratropics on 11 October 1996 at 12UTC. The 500 K surface was chosen because it lies in the lower stratosphere where much ozone depletion occurs during early austral spring, and hence where the transport and mixing of ozone-poor and ozone-rich air is very significant. The potential vorticity field shows a strong austral winter polar vortex south of about  $60^\circ\text{S}$ , with a well-mixed surf zone in the midlatitudes. Shedding of a filament is seen around  $90^\circ\text{E}$  in the  $\mathcal{P}$  field (cf. the  $-25$  PVU contour). Filament shedding is the hallmark of chaotic stirring in the stratosphere. The absolute vorticity field reveals that the polar vortex has a rich internal structure, as far as chaotic kinematics in the stratospheric flow is concerned [recall the direct relation between  $\zeta_\theta$  and the wind field in Eq. (14)]. There are two ridges of strong cyclonic absolute vorticity near the vortex edge, flanking a less cyclonic plateau at the vortex center. The ridged feature of the polar vortex will be seen to have important consequences on chaotic stirring within the vortex.

Let us examine the known elliptic trajectories on the 500 K surface first. These are the trajectories that satisfy the sufficient condition for Lagrangian ellipticity for some time interval that includes 12UTC 11 Oct 1996. Figure 3 shows these trajectories obtained from 9-day advectons from 12UTC 11 Oct 1996 both forward and backward in time. The plot on the left shows the total time  $(\tau_b + \tau_f)$  for which these trajectories stayed continually in an elliptic region ( $|r| > 1$ ) straddling the time 12UTC 11 Oct 1996. The longest that the trajectories ever satisfy the sufficient condition for Lagrangian ellipticity is only 2.6 days. However, this does *not* mean that the trajectories are only elliptic for up to 2.6 days, but that the sufficient condition is too strong to detect the ellipticity beyond this time. A prominent streak of elliptic trajectories is present just outside the polar vortex in the sector ( $0^\circ\text{E}, 60^\circ\text{E}$ ). A smaller streak is also present on the diametrically opposite side of the polar vortex. These elliptic coherent structures, as Haller<sup>39</sup> labels them, are aligned parallel to the strong absolute vorticity ridges in the vortex. They survive for at least about 1 day, as far as we know from the present (rather strong) sufficient condition for Lagrangian ellipticity. Elliptic coherent structures are barriers to transport and so we estimate that the barrier to cross-edge transport in the polar vortex has a minimum leakage time of  $\geq 1$

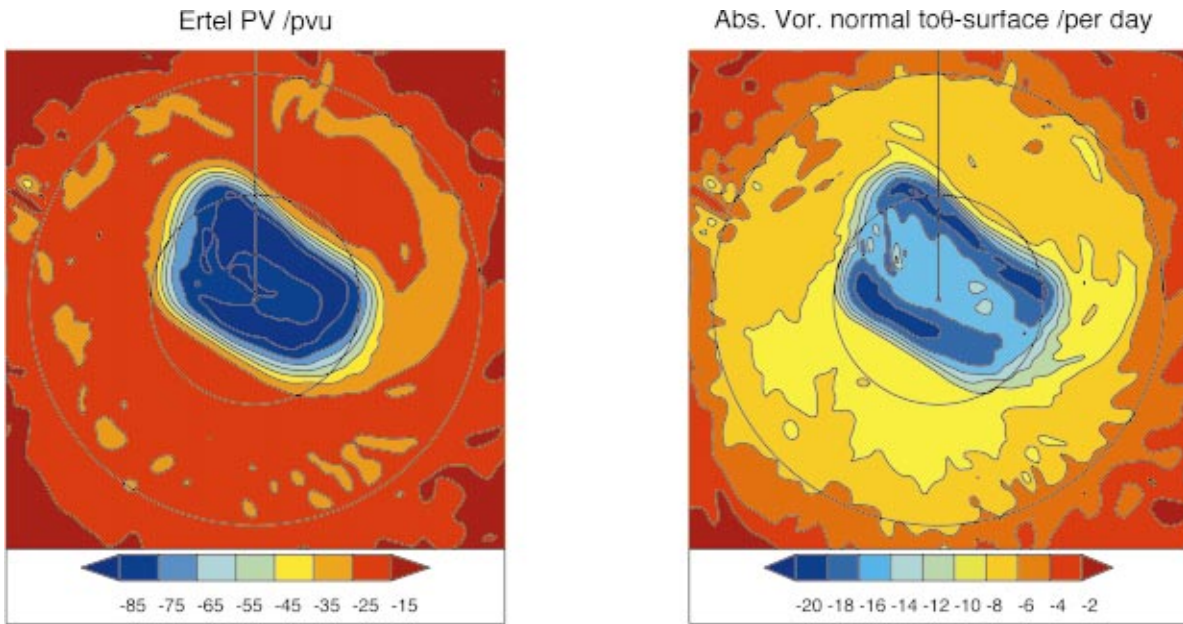


FIG. 2. (Color) Distribution of potential vorticity  $\mathcal{P}$  (left) and absolute vorticity  $\zeta_\theta$  (right) on the 500 K isentropic on 11 Oct 1996 at 12UTC. Here and in Figs. 3–6, the  $0^\circ$  meridian is denoted by a straight black line, the latitudes  $30^\circ\text{S}$  and  $60^\circ\text{S}$  are demarcated by closed circles, and stereographic projections are used. Potential vorticity units are in PVU ( $1\text{ PVU} = 10^{-6}\text{ K kg}^{-1}\text{ m}^2\text{ s}^{-1}$ ).

day, which is undoubtedly an excessively low bound based on our current knowledge of the polar vortex.

The plot on the right-hand side of Fig. 3 shows  $\log_{10}(\int |\phi_0| dt)$  over the period for which the particles satisfy the sufficient condition for Lagrangian ellipticity. Recall that the integral  $\int |\phi_0| dt$  denotes the lower-limit estimate of the total angular rotation of the local flow around an elliptic trajectory. (The use of logarithm in Fig. 3 and subsequent figures is in order to reflect the wide range of plotted values.) For the two elliptic coherent structures just outside the polar

vortex,  $\int |\phi_0| dt \approx \pi$  (or  $\log_{10}(\int |\phi_0| dt) \approx 0.50$ ) means that neighboring particles in these structures vascillate toward and away from one another at least once. Other patches of elliptic trajectories are seen in Fig. 3, but it is difficult to see if they are definitely associated with dynamical flow features such as cyclonic vorticity patches because of the noisy nature of vorticity data. We may perhaps speculate that their location at around  $30^\circ\text{S}$  is associated with the subtropical transport barrier.<sup>44</sup>

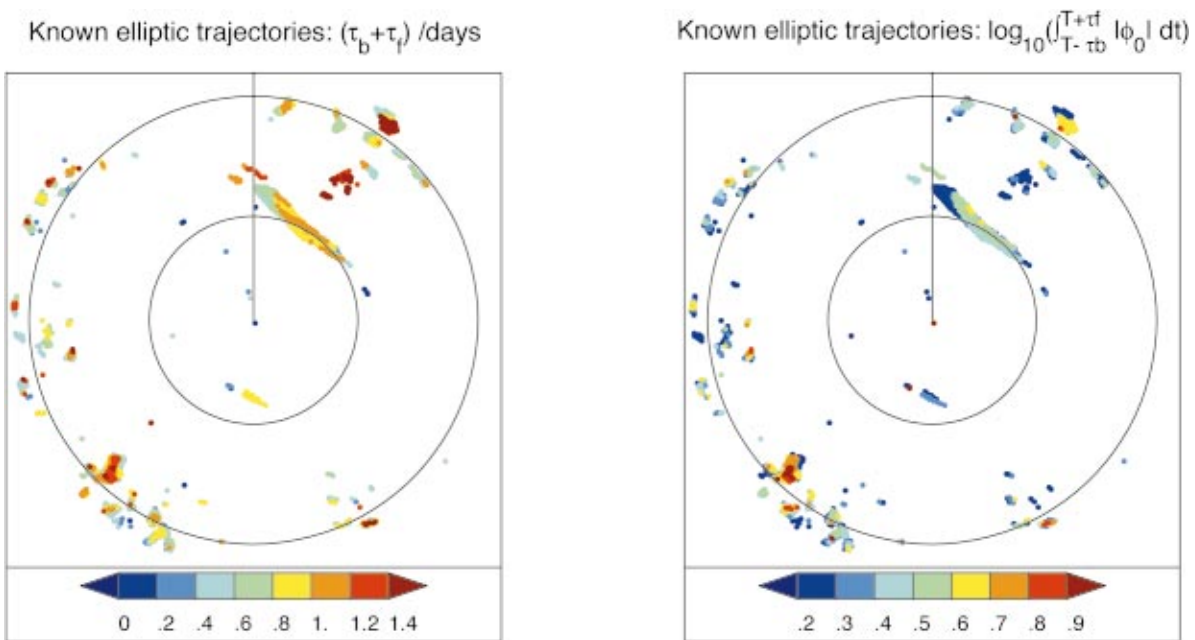
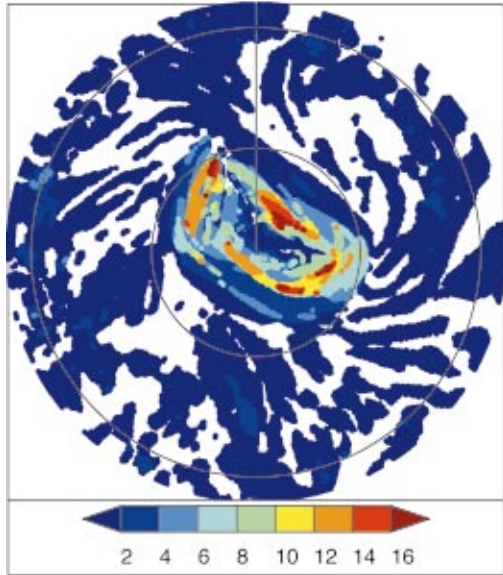


FIG. 3. (Color) Trajectories satisfying the sufficient condition for Lagrangian ellipticity for some time interval including 12UTC 11 Oct 1996. Left-hand panel: period  $(\tau_b + \tau_f)$  for which the elliptic trajectories stay in an elliptic region; right-hand panel:  $\log_{10}(\int |\phi_0| dt)$  for this period.

Known hyperbolic trajectories:  $(\tau_b + \tau_f)$  /days



Known hyperbolic trajectories:  $\log_{10}(\int_{T-\tau_b}^{T+\tau_f} \Lambda dt)$

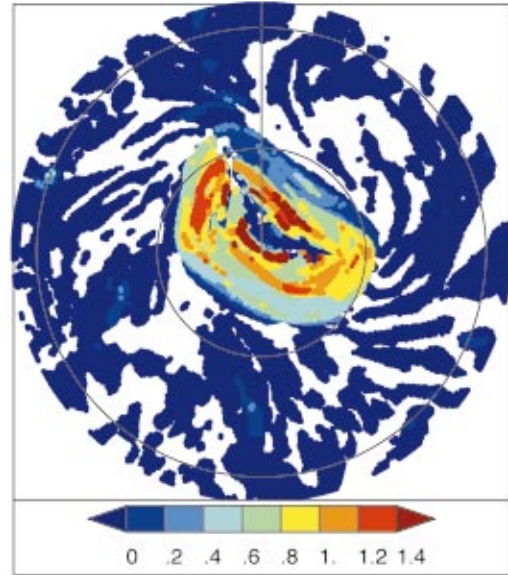


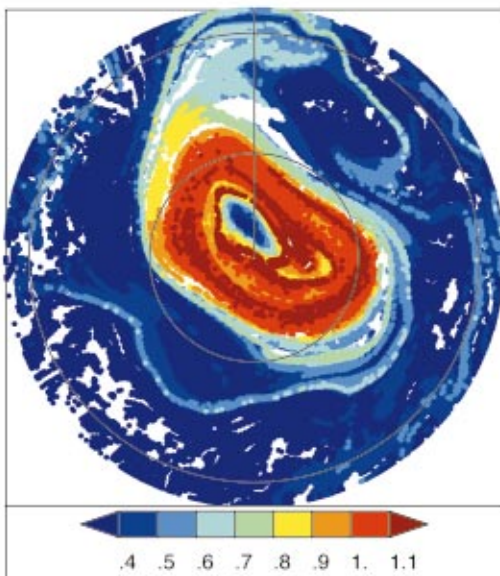
FIG. 4. (Color) Trajectories satisfying the sufficient condition for Lagrangian hyperbolicity for some time interval including 12UTC 11 Oct 1996. Left-hand panel: time spent in hyperbolic regions,  $(\tau_b + \tau_f)$ ; right-hand panel: strength of hyperbolicity over this time, measured by  $\log_{10}(\int \Lambda dt)$ .

Figure 4 shows the trajectories on the 500 K surface that satisfy the sufficient condition for Lagrangian hyperbolicity for some time interval that includes 12UTC 11 Oct 1996. Again, results from 9-day forward- and backward-time advections from 12UTC 11 Oct 1996 have been combined. The left-hand plot shows the total time  $(\tau_b + \tau_f)$  spent in hyperbolic regions (i.e.,  $|r| < 1$ ); the right-hand plot shows the strength of the hyperbolicity, denoted by  $\log_{10}(\int \Lambda dt)$  computed over this time [cf. Eq. (18) for the definition of  $\Lambda$ ]. Evidently, the trajectories that satisfy the sufficient condition for the longest time and experience the strongest hyperbolic-

ity all lie within the polar vortex. This indicates persistent and strong stirring within the polar vortex that we attribute to the presence of the two strong cyclonic absolute vorticity ridges within the polar vortex seen in Fig. 2 (right-hand plot). As for the filament-shedding seen in Fig. 2 (left-hand plot), we expect to see the hyperbolic trajectories responsible for this event to lie outside the polar vortex.<sup>37,45</sup> However, it appears that the sufficient condition is too strong to detect these hyperbolic trajectories.

Next, we examine the trajectories satisfying the necessary condition for Lagrangian hyperbolicity. In Fig. 5, all

Candidate hyp traj: Forw  $\tau_n=9$ days,  $\log_{10}(\int_{T-9}^{T+9} \Lambda dt)$



Candidate hyp traj: Back  $\tau_n=9$ days,  $\log_{10}(\int_{T-9}^{T} \Lambda dt)$

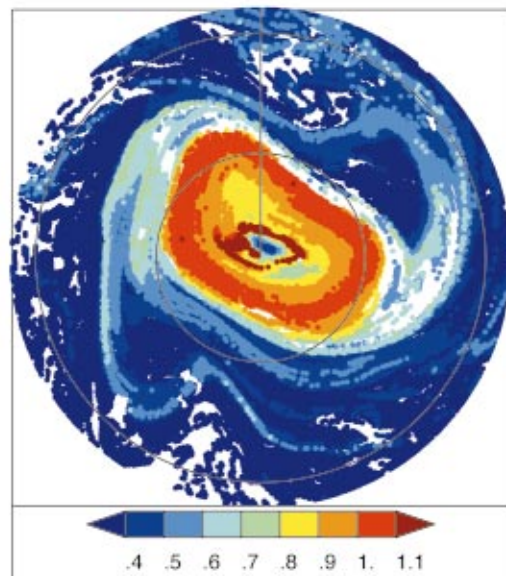


FIG. 5. (Color) Trajectories satisfying the necessary condition for Lagrangian hyperbolicity for  $\tau_n=9$  days in forward-time (left-hand side) and backward-time (right-hand side) advection from 12UTC 11 Oct 96. The colors indicate  $\log_{10}(\int \Lambda dt)$  over the 9 days.

particles plotted satisfy the necessary condition for the full 9-day duration of forward-time (left-hand plot) and backward-time (right-hand plot) advections from 12UTC 11 Oct 1996. Some subset of these particles is the set of all hyperbolic trajectories for the 9-day period of forward-time (left-hand plot) and backward-time (right-hand plot) advection. To estimate the location of this subset, we color-coded each particle with the value of  $\log_{10}(\int \Lambda dt)$  computed along its trajectory for the 9 days in forward (left-hand plot) and backward (right-hand plot) time, where  $\Lambda$  is given by Eq. (18). The particles with higher  $\log_{10}(\int \Lambda dt)$  (i.e., warmer colors in Fig. 5) are good candidates for hyperbolic trajectories, as they experience strong local hyperbolicity during the 9 days. However, we still cannot identify these candidate hyperbolic trajectories as hyperbolic trajectories proper, because they only satisfy the necessary condition. Nonetheless, the clustering of candidate hyperbolic trajectories within the polar vortex is consistent with the same clustering of hyperbolic trajectories in the polar vortex detected by the sufficient condition in Fig. 4. Moreover, the cyan-green regions in Fig. 5 provide convincing indications of hyperbolic lines in the stratospheric flow: two repelling lines (left-hand plot) and two attracting lines (right-hand plot) are located on diametrically opposite sides of the polar vortex. We explain next how we know that the hyperbolic lines picked out in Fig. 5 are repelling in the left-hand plot, and attracting in the right-hand plot.

Because fluid volume is conserved in nondivergent flows, repelling lines shorten as they repel the surrounding fluid away from them. (This process is analogous to flattening a ball of putty: the putty becomes short as its circumference expands outwards.) The shortening of the repelling lines in the left-hand plot of Fig. 5 brings the particles on the lines closer to the polar vortex, where there is stronger local hyperbolicity. Therefore, repelling lines show up with high values of  $\int \Lambda dt$ . In contrast, attracting lines lengthen as they attract the surrounding fluid, and so carry the particles on them away from the polar vortex. Thus, the values of  $\int \Lambda dt$  remain low on attracting lines, making attracting lines unnoticeable in the left-hand plot of Fig. 5. However, attracting lines shorten in reverse time, and therefore, they (and not the repelling lines) show up with high values of  $\int \Lambda dt$  in the right-hand plot of Fig. 5. Beware that the attracting and repelling lines revealed in Fig. 5 apply to different time periods: 9 days before and 9 days after 12UTC 11 Oct 1996, respectively.

One attracting line in Fig. 5 (right-hand plot) is collocated with the filament breaking in Fig. 2 (left-hand plot). But paradoxically, there are no filaments associated with the other attracting line in Fig. 5 (right-hand plot). This point illustrates the complex relation between tracer filaments and attracting lines: on one hand, attracting lines encourage tracers in the polar vortex to break outward via the mechanism of lobe dynamics<sup>30,45</sup> thereby forming filaments. On the other hand, filament-shedding erodes the polar vortex, causing the vortex edge to retreat polewards. Thus, the tracers in the vortex eventually get beyond the reach of the attracting lines, preventing further filament-breaking. (Of course, on longer time scales, vertical advection and tracer sources will have to

restore the equatorward reach of the polar vortex to accomplish a quasiequilibrium situation with intermittent filament shedding.)

In contrast to attracting lines, the repelling lines in Fig. 5 (left-hand plot) are not associated with any obvious tracer features in Fig. 2 (left-hand plot). This is not surprising, as repelling lines represent well-mixed surf-zone air that will be entrained into the vortex-edge region, also called the *stochastic layer* in Ref. 37. As such, identification of repelling lines in the surf zone using dynamical-system methods is all the more significant, as they locate the otherwise unmarked sources of surf-zone air for the vortex-edge region.

We repeated the computations of candidate hyperbolic trajectories for shorter and longer advections to test the sensitivity of  $\int_I \Lambda dt$  to the length of time interval  $I$ , and hence gauge the suitability of  $\int_I \Lambda dt$  as a marker of hyperbolic lines in stratospheric flow. Figure 6 shows the trajectories satisfying the necessary condition for Lagrangian hyperbolicity for 5-day (left) and 18-day (right) forward-time advections from 12UTC 11 Oct 1996. The colors denote  $\log_{10}(\int \Lambda dt)$  for the corresponding 5-day and 18-day periods, using the same color scale as Fig. 5. The left-hand plot shows that 5 days is too short for  $\log_{10}(\int \Lambda dt)$  to pick out the hyperbolic lines. This signifies that the time scale for chaotic stirring in the stratosphere is longer than 5 days. Comparing the right-hand plot of Fig. 6 and the left-hand plot of Fig. 5, we see that both 9-day and 18-day advections pick out practically the same hyperbolic lines. Hence, we deduce that the  $\int \Lambda dt$  statistics have probably converged for  $\tau_n \geq 9$  days and the hyperbolic lines thus picked out by high  $\int \Lambda dt$  values are robust features of the stratospheric flow.

In addition to above-mentioned case study surrounding the filament-shedding event of 12UTC 11 Oct 96, we performed a similar case study using 5-, 9-, and 18-day forward-time and backward-time integrations from 12UTC 21 Oct 96. The results obtained were similar to the presented case study in this paper.

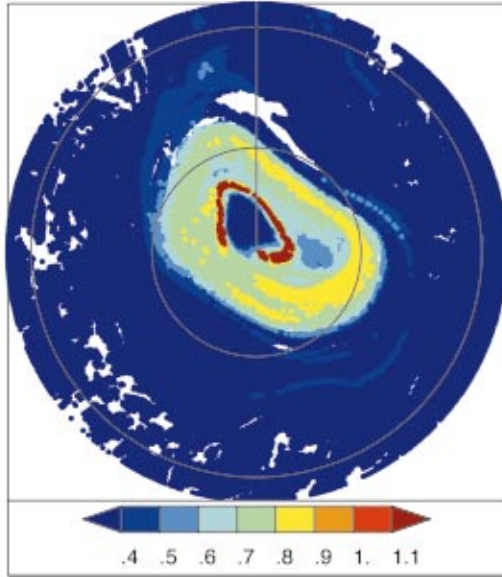
## VI. FINITE-SIZE LYAPUNOV EXPONENTS

In order to compare the results of rigorous Haller's conditions with that of other, nonrigorous, methods, we present here calculations of the *finite-size Lyapunov exponent* (FSLE) first used for dispersion by Artale *et al.*<sup>46</sup> and already applied to the polar stratosphere in Refs. 37 and 47. The goal of the various methods mentioned in Sec. I of this work is either to estimate the local stirring properties of the fluid or to draw the skeleton of the hyperbolic properties of the flow, that is to find the main stable and unstable hyperbolic lines. As we shall see in the following, the FSLE provides information on both aspects by varying a unique internal parameter.

The FSLE is based on the finite dispersion of particle pairs. For a given finite initial separation  $\delta(\mathbf{x}, t, 0) = \delta_0$  at time  $t$  and a growth factor  $\rho$ , the FSLE is

$$\lambda_\rho(\mathbf{x}, t, \delta_0) = \frac{1}{\tau} \ln \rho, \quad (19)$$

Candidate hyp traj: Forw  $\tau_n=5$ days,  $\log_{10}(\int_0^T \Lambda dt)$



Candidate hyp traj: Forw  $\tau_n=18$ days,  $\log_{10}(\int_0^T \Lambda dt)$

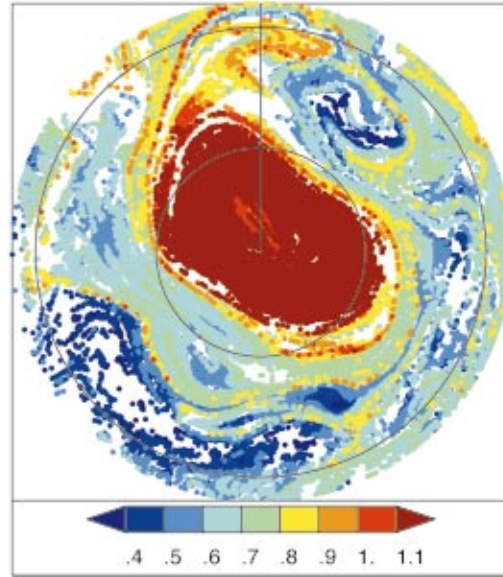


FIG. 6. (Color) Trajectories satisfying the necessary condition for Lagrangian hyperbolicity for  $\tau_n = 5$  days (left-hand side) and  $\tau_n = 18$  days in forward-time advection from 12UTC 11 Oct 96. The colors indicate  $\log_{10}(\int \Lambda dt)$  over the  $\tau_n$  days.

where  $\tau$  is such that the separation at time  $t + \tau$  is  $\delta(\mathbf{x}, t, \tau) = \rho \delta_0$ . Hence  $\tau$  is the required time to increase the separation by a factor  $\rho$ . When  $\rho$  is of the order of a few units,  $\lambda$  describes the stirring properties at scale  $\delta_0$  and can be interpreted as the inverse of a local turbulence time.<sup>46,48</sup> One expects this time to be highly scale dependent in three-dimensional turbulence but its scale dependence should be weak, at most logarithmic, for layerwise motion governed by quasigeostrophic dynamics.<sup>49</sup> When  $\rho \gg 1$ , the unstable and stable hyperbolic material lines are obtained by plotting the extrema of  $\lambda$  for, respectively, forward- and backward-time advectons. Here the resolution  $\delta_0$  is limited by the need to grow the separation to synoptic scale within a duration  $\tau$  of the order of the integral scale.

The advantage of using the FSLE instead of the plain dispersion [proposed by Bowman<sup>50</sup> and obtained by letting  $\tau$  be fixed and measuring  $\delta(\mathbf{x}, t, \tau)$ ] has been discussed in Ref. 37. The basic reason is that plain separation is liable to saturation effects and provides a “fuzzy” view of the hyperbolic structure compared to FSLE. It has been shown in several examples of dynamical systems that FSLE maps the stable and unstable hyperbolic manifolds.<sup>37</sup>

Our implementation of the FSLE method is as follows. First, we initialize a quasiuniform grid of particles in the flow domain, which is the 500 K isentropic surface from 25°S to the pole. Considering  $N = 260$  equally spaced parallels in this latitude range separated by  $\Delta\phi = 0.25^\circ$ , we put  $(2\pi/\Delta\phi)\cos\phi$  regularly spaced points on each circle of latitude  $\phi$ , resulting in  $M = 191074$  points to cover the latitude range with a resolution of 26 km. Then, we consider for each point of the reference distribution four perturbed points at arc-distance  $1/2\delta_0 = 0.05^\circ$  in the four cardinal directions. This generates two pairs separated by 11 km in the meridional and zonal directions around each point  $\mathbf{x}_j$  of the grid. Then, we calculate the evolution of the four particles forward

and backward in time from time  $t$  and we measure the pair separation at time  $t + \tau$  corresponding to point  $\mathbf{x}_j$  as the maximum arc-distance among the two pairs initialized around  $\mathbf{x}_j$  at time  $t$ . We check the times  $\tau_{ij}$  at which this pair separation first crosses predefined threshold distances given by  $\delta_i = \rho_i \delta_0$ , where  $\rho_i$  is chosen among  $\{5, 10, 20, 50, 75, 100\}$ . Then, we use Eq. (19) to define the FSLE  $\lambda_{\rho_i}(\mathbf{x}_j, t, \delta_0) = \log \rho_i / \tau_{ij}$ . If a threshold distance is not reached by the particle in the finite-time of consideration (20 days in our calculations), FSLE values are zeroed out for such least stretching points and this threshold. Finally, we map the FSLE values onto the initial locations of points in the reference distribution.

Figure 7 shows the FSLE chart for a growth ratio  $\rho = 100$ . Here only the points with largest  $\lambda_{100}$  are plotted. They are distributed along well-defined alignments which are good candidates for the main hyperbolic lines of the flow. They agree with the lines of maximum hyperbolicity strength in Fig. 5. The stable and unstable lines intersect many times in particular within the collar around the vortex, generating a number of lobes. It was shown in Ref. 37 that the lobes within the collar are associated with the turnstile mechanism of fluid going in and out the collar along the hyperbolic lines.

Figure 8 shows FSLE charts for 20 days forward and backward integrations from 12 UTC 11 Oct 1996 and a growth ratio  $\rho = 5$ . The white patches show the regions where the separation has grown over less than a factor 5 over 20 days. Since  $\lambda_5 = 0.179 \text{ day}^{-1}$  for  $\tau = 9$  days, we see that the pairs separating between 9 and 20 days are shown by the lowest colors in each chart. Therefore, the main patterns of Fig. 8 are obtained for  $\tau < 9$  days, that is over the optimal duration found for the necessary hyperbolic condition in Sec. V. Integrating over 20 days only add details in the weakly stretched regions. In both forward and backward directions,

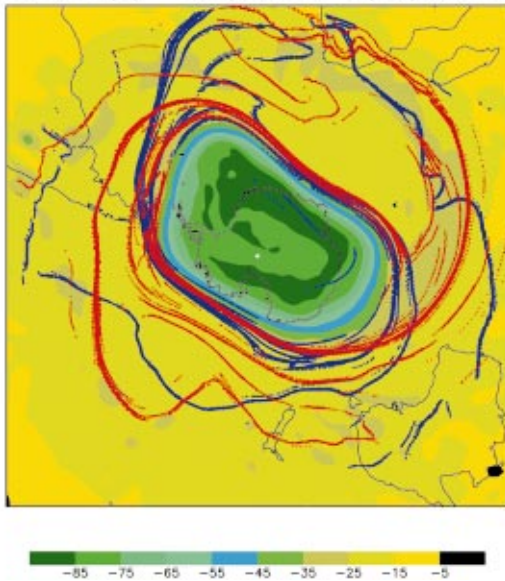
PV & FSLE (+/- 10 d), 500 K, 11/10/96,  $r=100$ 

FIG. 7. (Color) FSLE for growth ratio  $\rho=100$  at 12UTC 11 Oct 96 for backward (red) and forward (blue) time advection. The selected points are those which reach the required separation within less than 10 days. PV is shown in the background according to the color scale.

the vortex edge is visible as a well-defined minimum in  $\lambda_5$  that follows approximately the location of the maximum PV gradient on the vortex edge, revealing a thin continuous barrier around the vortex that the sufficient ellipticity condition failed to capture. (There is also a region of small  $\lambda_5$  sitting at the core of the vortex indicating weak mixing in this region in agreement with the results shown in Fig. 5.)

The vortex is surrounded by a collar with large values of  $\lambda_5$ , the largest values being located near the tips of the vortex from which arms detach and expand within the midlatitude surf zone. In Fig. 8 (right-hand side), the broadest arm

extends along the PV filament being expelled from the vortex. This arm and the others agree with the locations of the hyperbolic lines detected in Fig. 5. These results suggest that mixing in the extratropical winter stratosphere is maximal within a collar surrounding the polar vortex and in a broadband along the hyperbolic lines connecting this collar to the surf zone. It was shown in Ref. 37 that fast two-way exchanges occur between the surf zone and the collar along the hyperbolic lines, with time scales of the order of 2–3 days. It is clear here that this mechanism is to a large extent disconnected from the exchanges across the vortex edge which occur over much longer time scales (see Sec. VII).

## VII. CONCLUSION AND DISCUSSION

We have shown that the application of rigorous Lagrangian hyperbolicity criteria provides *per se* limited insight on the dynamics of the Antarctic stratospheric polar vortex. This is not totally surprising since the proofs of these criteria contain severe approximations of the hyperbolic properties of the flow (see Ref. 39). The mere existence of such criteria which can be applied and tested with real observed winds is, however, a significant result. In practice, improved phenomenological criteria can be derived by measuring the strength of hyperbolicity or from the properties of pair separation. The apparent success of these nonrigorous methods in revealing the hyperbolic structure of the flows, here in the atmosphere, but also in numerical and experimental turbulent flows,<sup>39,51</sup> clearly calls for further theoretical development to explain these results. One possibility is to improve the necessary and sufficient conditions for hyperbolicity and ellipticity. Another possibility, recently considered in Ref. 52 is to provide a rigorous way to test the hyperbolic nature of a candidate hyperbolic line once it has been found by any convenient method. It would be very interesting to apply such tests to FSLE.

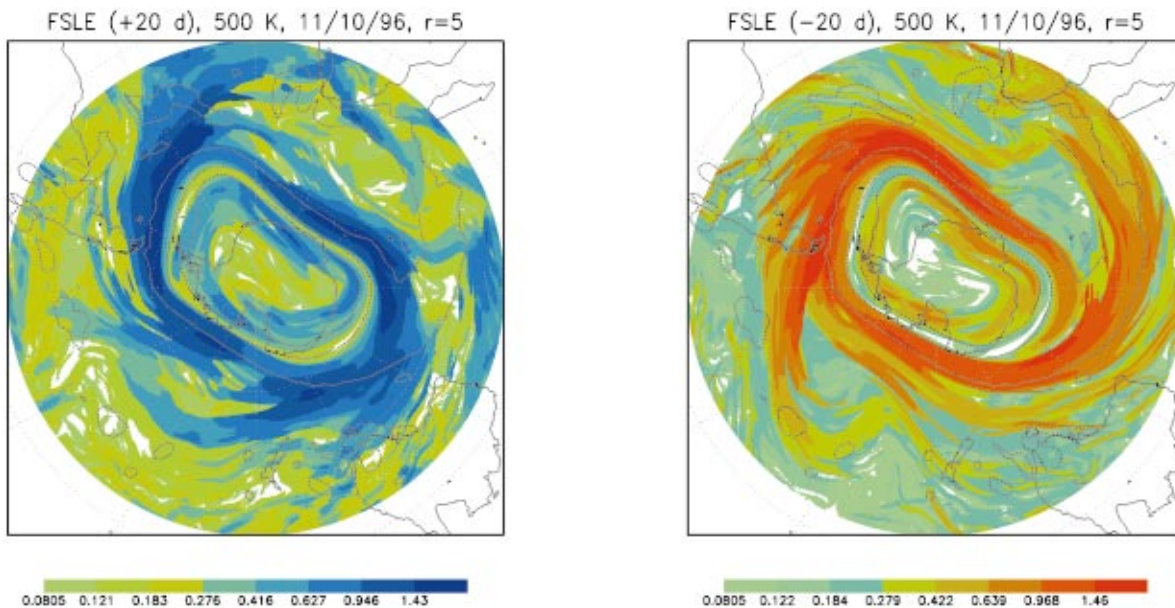


FIG. 8. (Color) FSLE for growth ratio  $\rho=5$  at 12UTC 11 Oct 96 for forward (left-hand side) and backward (right-hand side) time advection. The colors indicate  $\lambda_5$  with logarithmic scaling. PV contours  $-25$ ,  $-55$  and  $-75$  PVU are plotted in dashed lines. The projection is the same as in previous figures.

The determination of the hyperbolic structures leads in principle to the possibility to calculate isentropic transport in the stratosphere using lobe dynamics. A first complication is that one has to distinguish not only the vortex and the surf zone but also a collar surrounding the vortex. A second complication is that stable and unstable material lines are almost parallel within the collar region, hence many lobes are very elongated and difficult to identify owing to numerical inaccuracies. A third difficulty is that the finite-time hyperbolic material lines do not necessarily need to cross and form lobes in aperiodic flows. In practice it seems that this technique may apply to the calculation of the exchanges between the collar and the surf zone but is hardly applicable to the much weaker exchanges between the polar vortex and its exterior.<sup>37,45</sup>

Another possibility to derive exchange coefficients is to interpret the FSLE for small  $\rho$  as the inverse of a local mixing time. The findings provided by Fig. 8 are indeed similar in several respects to those obtained by *effective diffusivity*.<sup>53</sup> In particular, effective diffusivity identifies the vortex edge barrier as a minimum, and there is a maximum located just equatorward of it. The advantage of effective diffusivity is that it is based on a rigorous equation obtained by averaging the advective diffusive equation along a tracer contour;<sup>54</sup> its drawback is to assume that a single value of effective diffusivity is valid all along a tracer contour, however the tracer contour deforms. In contrast, the FSLE is defined independently of the tracer concentration and its contours are clearly crossing the PV contours in many instances. The tendency of tracer contours to align with hyperbolic lines<sup>24</sup> induces, however, alignment of FSLE contours and tracer contours at the vortex edge and the surrounding collar. Normally,  $\lambda_5$  is partly due to the effect of the shear along tracer lines which results in practically no mixing. So,  $1/\lambda_5$  is usually a lower bound of the mixing time. But at the vortex edge, the effect of the shear is limited because the edge is also close to a maximum of the horizontal wind. The FSLE indicates that the exchange time between the interior and the exterior of the vortex is of the order of 3 weeks at least.

**ACKNOWLEDGMENT**

T.Y.K. acknowledges the support of a fellowship from Ecole Polytechnique during his visit at LMD.

**APPENDIX: THE EXPRESSION FOR  $|\phi_0|$**

Haller<sup>39</sup> defines

$$\phi_0 \equiv \min[\phi^+, \phi^-], \tag{A1}$$

$$\phi^\pm \equiv \frac{1}{2} \frac{\langle \xi^\pm, \mathbf{M} \xi^\pm \rangle}{|\xi^\pm| |\mathbf{S} \xi^\pm|}, \tag{A2}$$

$$\mathbf{M} \equiv 2\mathbf{S} \cdot \nabla \mathbf{v} + \dot{\mathbf{S}}_{\text{nrot}},$$

where  $(\xi^+, \xi^-)$  is the zero-strain set and  $\dot{\mathbf{S}}_{\text{nrot}}$  is the rate of change of the strain matrix  $\mathbf{S}$  in a nonrotating frame of reference. In spherical coordinates, the rate of change of the strain matrix  $\dot{\mathbf{S}}$  is

$$\dot{\mathbf{S}} = \dot{\mathbf{S}}_{\text{nrot}} + \dot{\mathbf{S}}_{\text{basis}}, \tag{A3}$$

where  $\dot{\mathbf{S}}_{\text{basis}}$  is the apparent rate of change that arises from the rotating basis set  $(\hat{\lambda}, \hat{\varphi})$  along a trajectory. Hence,

$$\mathbf{M} \equiv 2\mathbf{S} \cdot \nabla \mathbf{v} + \dot{\mathbf{S}} - \dot{\mathbf{S}}_{\text{basis}}. \tag{A4}$$

First, consider that the unit vector  $\hat{\lambda}$  rotates by  $\mu \dot{\lambda} \delta t$  in the tangential plane of the spherical surface over time  $\delta t$ , where  $\mu \equiv \sin \varphi$ . Hence, the change in  $\mathbf{S}$  due to the rotation of the basis is

$$\delta \mathbf{S}_{\text{basis}} = \epsilon \mathbf{S} \epsilon^{-1} - \mathbf{S}, \tag{A5}$$

where

$$\epsilon \equiv \begin{pmatrix} \cos(\mu \dot{\lambda} \delta t) & \sin(\mu \dot{\lambda} \delta t) \\ -\sin(\mu \dot{\lambda} \delta t) & \cos(\mu \dot{\lambda} \delta t) \end{pmatrix}.$$

To first order in  $\delta t$ ,

$$\epsilon \approx \begin{pmatrix} 1 & \mu \dot{\lambda} \delta t \\ -\mu \dot{\lambda} \delta t & 1 \end{pmatrix},$$

$$\epsilon^{-1} \approx \begin{pmatrix} 1 & -\mu \dot{\lambda} \delta t \\ \mu \dot{\lambda} \delta t & 1 \end{pmatrix}.$$

Substituting the above into Eq. (A5), we get

$$\dot{\mathbf{S}}_{\text{basis}} \equiv \lim_{\delta t \rightarrow 0} \frac{\delta \mathbf{S}_{\text{basis}}}{\delta t} = 2\mu \dot{\lambda} \begin{pmatrix} b & -a \\ -a & -b \end{pmatrix}. \tag{A6}$$

Next, we substitute Eq. (A6) into Eq. (A4) to get

$$\mathbf{M} = \begin{pmatrix} 2\sigma^2 + 2b\Omega + a & -2a\Omega + b \\ -2a\Omega + b & 2\sigma^2 - 2b\Omega - a \end{pmatrix}. \tag{A7}$$

Now, the vectors  $\xi^\pm$  making up the zero strain set make an angle of  $\mp \pi/4$  with the strain axis  $E^+$ . Let  $E^+$  make an angle  $\vartheta$  with the  $\hat{\lambda}$  vector. Hence,

$$\xi^\pm = \begin{pmatrix} \cos(\vartheta \mp \pi/4) \\ \sin(\vartheta \mp \pi/4) \end{pmatrix}. \tag{A8}$$

Substituting Eqs. (A7) and (A8) into Eq. (A2), and then using the identities:  $a \equiv \sigma \cos 2\vartheta$ ,  $b \equiv \sigma \sin 2\vartheta$ , and recalling Eqs. (6) and (8), we get

$$\begin{cases} \langle \xi^\pm, \mathbf{M} \xi^\pm \rangle = 2\sigma^2 \pm 2(b\Omega + a) \sin 2\vartheta \pm (2a\Omega - b) \cos 2\vartheta \\ |\mathbf{S} \xi^\pm| = \sigma \end{cases}$$

$$\Rightarrow \phi^\pm = \sigma \pm (\Omega - \vartheta).$$

And using  $\Omega_{\text{eff}}$  defined in Eq. (7), Eq. (A1) becomes

$$\phi_0 = \min(\sigma + \Omega_{\text{eff}}, \sigma - \Omega_{\text{eff}}) = \min(\sigma + |\Omega_{\text{eff}}|, \sigma - |\Omega_{\text{eff}}|) = \sigma - |\Omega_{\text{eff}}|.$$

In an elliptic region,  $|\Omega_{\text{eff}}| > \sigma$  so that

$$|\phi_0| = |\Omega_{\text{eff}}| - \sigma.$$

<sup>1</sup>G. K. Batchelor, "Small-scale variation of convected quantities like temperature in turbulent fluid," J. Fluid Mech. **5**, 113–133 (1959).

<sup>2</sup>G. Falkovich, K. Gawędzki, and M. Vergassola, "Particles and fields in fluid turbulence," Rev. Mod. Phys. **73**, 913–975 (2001).

<sup>3</sup>E. Balkovsky and A. Fouxon, "Universal long-time properties of Lagran-

- gian statistics in Batchelor regime and their application to passive scalar problem," *Phys. Rev. E* **60**, 4164–4174 (1999).
- <sup>4</sup> Y. Hu and R. Pierrehumbert, "The advection-diffusion problem for stratospheric flow. I. Concentration probability distribution," *J. Atmos. Sci.* **58**, 1493–1510 (2001).
- <sup>5</sup> J. Cho and E. Lindborg, "Horizontal velocity structure functions in the upper troposphere and lower stratosphere. I. Observations," *J. Geophys. Res.*, [Atmos.] **106**, 10233–10232 (2001).
- <sup>6</sup> P. Chen, J. R. Holton, A. O'Neill, and R. Swinbank, "Quasi-horizontal transport and mixing in the Antarctic stratosphere," *J. Geophys. Res.*, [Atmos.] **99**, 16851–16866 (1994).
- <sup>7</sup> W. Randel, "Ideas flow on Antarctic polar vortex," *Nature (London)* **364**, 105–106 (1993).
- <sup>8</sup> G. Manney, R. Zurek, A. O'Neill, and R. Swinbank, "On the motion of air through the stratospheric polar vortex," *J. Atmos. Sci.* **51**, 2973–2994 (1994).
- <sup>9</sup> A. Sobel and R. Plumb, "Quantitative diagnostic of mixing in a shallow water model of the stratosphere," *J. Atmos. Sci.* **56**, 2811–2829 (1999).
- <sup>10</sup> A. Tuck, "Synoptic and chemical evolution of the Antarctic vortex in late winter and early spring," *J. Geophys. Res.*, [Atmos.] **94**, 11687–11737 (1989).
- <sup>11</sup> D. Waugh *et al.*, "Transport of material out of the stratospheric Arctic vortex by Rossby wave breaking," *J. Geophys. Res.*, [Atmos.] **99**, 1071–1088 (1994).
- <sup>12</sup> J. M. Ottino, *The Kinematics of Mixing: Stretching, Chaos and Transport* (Cambridge University Press, New York, 1989).
- <sup>13</sup> M. R. Schoeberl and P. A. Newman, "A multiple-level trajectory analysis of vortex filaments," *J. Geophys. Res.*, [Atmos.] **100**, 25801–25815 (1995).
- <sup>14</sup> D. Waugh *et al.*, "Mixing of polar air into middle latitudes as revealed by tracer-tracer scatter plots," *J. Geophys. Res.*, [Atmos.] **102**, 13119–13134 (1997).
- <sup>15</sup> P. Haynes and E. Shuckburgh, "Effective diffusivity as a diagnostic of atmospheric transport. I. Stratosphere," *J. Geophys. Res.*, [Atmos.] **105**, 22777–22794 (2000).
- <sup>16</sup> M. McIntyre and T. Palmer, "The surf zone in the stratosphere," *J. Atmos. Sci.* **46**, 825–849 (1984).
- <sup>17</sup> A. Mariotti, B. Legras, and D. Dritschel, "Vortex stripping and the erosion of coherent structures in two-dimensional flows," *Phys. Fluids* **6**, 3954–3962 (1994).
- <sup>18</sup> B. Legras, D. Dritschel, and P. Caillol, "The erosion of a distributed two-dimensional vortex in a background straining flow," *J. Fluid Mech.* **441**, 369–398 (2000).
- <sup>19</sup> A. Okubo, "Horizontal dispersion of floatable particles in the vicinity of velocity singularities such as convergences," *Deep-Sea Res. Oceanogr. Abstr.* **17**, 445–454 (1970).
- <sup>20</sup> J. Weiss, "The dynamics of enstrophy transfer in two-dimensional hydrodynamics," *Physica D* **48**, 273–294 (1991).
- <sup>21</sup> C. Basdevant and T. Philipovich, "On the validity of the 'Weiss criterion' in two-dimensional turbulence," *Physica D* **73**, 17–30 (1994).
- <sup>22</sup> B. Hua and P. Klein, "An exact criterion for the stirring properties of nearly two-dimensional flows," *Physica D* **113**, 98–110 (1998).
- <sup>23</sup> G. Lapeyre, P. Klein, and B. Hua, "Does the tracer gradient vector align with the strain eigenvectors in 2-D turbulence?" *Phys. Fluids* **11**, 3729 (1999).
- <sup>24</sup> P. Klein, B. L. Hua, and G. Lapeyre, "Alignment of tracer gradient vectors in 2D turbulence," *Physica D* **146**, 246 (2000).
- <sup>25</sup> G. K. Batchelor, "The effect of homogeneous turbulence on material line surfaces," *Proc. R. Soc. London, Ser. A* **213**, 349–366 (1952).
- <sup>26</sup> G. M. Zaslavsky, *Physics of Chaos in Hamiltonian Systems* (Imperial College Press, London, 1998).
- <sup>27</sup> V. Rom-Kedar, A. Leonard, and S. Wiggins, "An analytical study of transport, mixing and chaos in an unsteady vortical flow," *J. Fluid Mech.* **214**, 347–394 (1990).
- <sup>28</sup> D. Beigie, A. Leonard, and S. Wiggins, "Chaotic transport in the homoclinic and heteroclinic tangle regions of quasi-periodically forced two-dimensional flows," *Nonlinearity* **4**, 775–819 (1991).
- <sup>29</sup> D. Beigie, A. Leonard, and S. Wiggins, "Invariant manifold templates for chaotic advection," *Chaos, Solitons Fractals* **4**, 749–868 (1994).
- <sup>30</sup> N. Malhotra and S. Wiggins, "Geometric structures, lobe dynamics, and Lagrangian transport in flows with aperiodic time-dependence, with applications to Rossby wave flow," *J. Nonlinear Sci.* **8**, 401–456 (1999).
- <sup>31</sup> G. Haller and A. Poje, "Finite time transport in aperiodic flows," *Physica D* **119**, 352–380 (1998).
- <sup>32</sup> G. Haller, "Finding finite-time invariant manifolds in two-dimensional velocity fields," *Chaos* **10**, 99–108 (2000).
- <sup>33</sup> G. Haller and G. Yuan, "Lagrangian coherent structures and mixing in two-dimensional turbulence," *Physica D* **147**, 352–370 (2000).
- <sup>34</sup> C. Couliette and S. Wiggins, "Intergyre transport in a wind-driven, quasi-geostrophic double gyre: An application of lobe dynamics," *Nonlinear Processes in Geophysics* **7**, 59–85 (2000).
- <sup>35</sup> R. Pierrehumbert and H. Yang, "Global chaotic mixing on isentropic surfaces," *J. Atmos. Sci.* **50**, 2462–2480 (1993).
- <sup>36</sup> N. Malhotra, I. Mezic, and S. Wiggins, "Patchiness: A new diagnostic for Lagrangian trajectory analysis in time-dependent fluid flows," *Int. J. Bifurcation Chaos Appl. Sci. Eng.* **8**, 1053–1093 (1998).
- <sup>37</sup> B. Joseph and B. Legras, "On the relation between kinematic boundaries, stirring, and barriers for the Antarctic polar vortex," *J. Atmos. Sci.* **59**, 1198–1212 (2002).
- <sup>38</sup> G. Haller, "Distinguished material surfaces and coherent structures in three-dimensional fluid flows," *Physica D* **149**, 248–277 (2001).
- <sup>39</sup> G. Haller, "Lagrangian coherent structures and the rate of strain in two-dimensional turbulence," *Phys. Fluids* **13**, 3365–3385 (2001).
- <sup>40</sup> G. Batchelor, *An Introduction to Fluid Mechanics* (Cambridge University Press, Cambridge, 1967).
- <sup>41</sup> E. Dresselhaus and M. Tabor, "The stretching and alignment of material elements in general flow fields," *J. Fluid Mech.* **236**, 415–444 (1991).
- <sup>42</sup> K. Ide, D. Small, and S. Wiggins, "Distinguished hyperbolic trajectories in time dependent fluid flows: Analytical and computational approach for velocity fields defined as data sets," *Nonl. Proc. Geophys.* (to be published).
- <sup>43</sup> H. Akima, "A method of univariate interpolation that has the accuracy of a third-order polynomial," *ACM Trans. Math. Softw.* **17**, 341–366 (1991).
- <sup>44</sup> D. W. Fahey *et al.*, "In situ observations of NO<sub>y</sub>, O<sub>3</sub>, and the NO<sub>y</sub>/O<sub>3</sub> ratio in the lower stratosphere," *Geophys. Res. Lett.* **23**, 1653–1656 (1996).
- <sup>45</sup> T.-Y. Koh and R. Plumb, "Lobe dynamics applied to barotropic Rossby-wave breaking," *Phys. Fluids* **12**, 1518–1528 (2000).
- <sup>46</sup> V. Artale, G. Boffetta, A. Celani, M. Cencini, and A. Vulpiani, "Dispersion of passive tracers in closed basins: Beyond the diffusion coefficient," *Phys. Fluids* **9**, 3162–3171 (1997).
- <sup>47</sup> G. Lacorata, G. Redaelli, and G. Visconti, "Finite-scale Lyapunov exponents as Lagrangian diagnostics of barriers and filaments in the polar vortex," preprint (2001).
- <sup>48</sup> G. Boffetta, M. Celani, G. Lacorata, and A. Vulpiani, "Nonasymptotic properties of transport and mixing," *Chaos* **10**, 50–60 (2000).
- <sup>49</sup> U. Frisch, *Turbulence: The Legacy of A. N. Kolmogorov* (Cambridge University Press, Cambridge, 1995).
- <sup>50</sup> K. P. Bowman, "Manifold geometry and mixing in observed atmospheric flows," *J. Atmos. Sci.* (submitted).
- <sup>51</sup> G. Voth, G. Haller, and J. P. Gollub, "Experimental measurements of stretching fields in fluid mixing," *Phys. Rev. Lett.* (to be published).
- <sup>52</sup> G. Haller, "Lagrangian coherent structures from approximate velocity data," *Phys. Fluids* **14**, 1851–1861 (2002).
- <sup>53</sup> A. M. Lee, H. K. Roscoe, A. E. Jones, P. H. Haynes, E. F. Shuckburgh, M. W. Morrey, and H. C. Pumphrey, "The impact of the mixing properties within the Antarctic stratospheric vortex on ozone loss in spring," *J. Geophys. Res.*, [Atmos.] **106**, 3203–3211 (2001).
- <sup>54</sup> N. Nakamura, "Two-dimensional mixing, edge formation, and permeability diagnosed in an area coordinate," *J. Atmos. Sci.* **53**, 1524–1537 (1996).